



Assessing methane emissions from collapsing Venezuelan oil production using TROPOMI

Brian Nathan¹, Joannes D. Maasackers¹, Stijn Naus¹, Ritesh Gautam², Mark Omara², Daniel J. Varon³, Melissa P. Sulprizio³, Alba Lorente¹, Tobias Borsdorff¹, Robert J. Parker^{4,5}, and Ilse Aben^{1,6}

¹SRON Netherlands Institute for Space Research, Leiden, The Netherlands

²Environmental Defense Fund, Washington DC, USA

³School of Engineering and Applied Sciences, Harvard University, Cambridge, MA, United States

⁴National Centre for Earth Observation, University of Leicester, Leicester, UK

⁵Earth Observation Science, School of Physics and Astronomy, University of Leicester, Leicester, UK

⁶Department of Earth Sciences, Vrije Universiteit Amsterdam, Amsterdam, The Netherlands

Correspondence: Brian Nathan (Dr.Brian.Nathan@gmail.com)

Abstract. Venezuela has long been identified as an area with large methane emissions, especially in the Lake Maracaibo region with intensive oil exploitation, but production has strongly decreased in recent years. The area is notoriously difficult to observe from space due to its complex topography and persistent cloud cover. We use the unprecedented coverage of the TROPospheric Monitoring Instrument (TROPOMI) methane observations in analytical inversions at the national scale with the Integrated Methane Inversion (IMI) framework and at regional scale with the Weather Research and Forecasting (WRF) model. In the IMI analysis, we find 2019 Venezuelan emissions of 7.5 (5.7-9.3) Tg a⁻¹, where about half of emissions can be informed by TROPOMI observations and emissions from oil exploitation are a factor ~1.6 higher than in bottom-up inventories. Using WRF, we find 2019 emissions of 1.2 (1.0 - 1.5) Tg a⁻¹ from the Lake Maracaibo area, close to bottom-up estimates. Our WRF estimate is ~40% lower than the regional result from the IMI due to differences in the meteorology used by the two models. We only find a small, non-significant, trend in emissions between 2018 and 2020 around the lake, implying the area's methane emission intensity expressed against oil/gas production has doubled over the time period to ~20%. This value is much higher than what has previously been found for other oil/gas production regions and indicates there could be large emissions from abandoned infrastructure.

1 Introduction

Venezuela has long been identified as a region with large methane emissions from its major oil production industry (Bergamaschi et al., 2007, 2009; Frankenberg et al., 2011). The area near Lake Maracaibo in the northwest of the country is specifically of interest as it is home to extensive oil production (Rystad Energy, 2022). Recently, Venezuela's oil production has steeply declined (U.S. Energy Information Administration, 2020). The region is also notoriously difficult to observe from space because of its proximity to the ocean, steep elevation gradients, and persistent cloud cover. The TROPospheric Monitoring Instrument (TROPOMI) satellite instrument (Veefkind et al., 2012) with its unprecedented combination of daily global coverage

and city-scale spatial resolution provides a new opportunity to address these methane emissions and their recent trends. We use TROPOMI methane data in inversions of two chemical transport models, one at country and one at the regional scale, to analyze 2018-2020 emissions in Venezuela with a specific focus on the Lake Maracaibo region.

25

Venezuela has historically been one of the largest oil producers in the world and as of 2020 had the largest national oil reserves (U.S. Energy Information Administration, 2020). The area around Lake Maracaibo (8.3-11.1 °N, 72.7-69.9 °S), a large tidal estuary in the northwest of the country, is one of the main oil-producing areas. The area was responsible for 30% of the country's oil production in 2012, with additional production happening in the remainder of the Maracaibo basin (Rystad Energy, 2022; Escalona and Mann, 2006). The area features both onshore as well as offshore production on the lake, where large oil spills have been detected in space-based visual imagery (Hu et al., 2003). The lake is surrounded by mountains and often covered by clouds while the wind tends to blow air south from the equator across the lake towards the mountains (González-Longatt et al., 2014). Oil is also produced in Venezuela's Orinoco basin in the eastern part of the country. While national oil production was steady around 2.5 million barrels per day in the 2000s and early 2010s, it strongly decreased in recent years as a result of U.S. sanctions and reduced capital expenditures. Production was only about 1.6 million barrels a day in 2018 and decreased to 0.7 million barrels a day in 2020 (Rystad Energy, 2022). Gas production remained relatively stable at ~0.4 million barrels of oil equivalent per day for 2018-2020 (Rystad Energy, 2022). Compared to 2018, oil production in the Lake Maracaibo area decreased by 60% in 2020, to 135 thousand barrels a day (Rystad Energy, 2022), and abandonment and decay of the production infrastructure has been widely reported (AP News, 2019; NASA, 2021). Gas production accounts for less than 5% of the area's oil/gas production (in energy equivalent). When Venezuela last reported emissions to the UNFCCC in 2017 (República Bolivariana De Venezuela, 2017), over 70% of total 2010 methane emissions (5 Tg a⁻¹) came from oil production. Other major sources included agriculture (24%) and waste (5%), while emissions from natural gas production were estimated to be less than 1 Gg a year. As more recent reports are not available, the global Scarpelli et al. (2022) inventory has to rely on an extrapolation based on production to estimate oil/gas emissions of 1.12 Tg a⁻¹ for 2019, with 0.79 Tg a⁻¹ located in the Maracaibo area.

45

Starting with the SCanning Imaging Absorption SpectroMeter for Atmospheric CHartography (SCIAMACHY, 2003-2014 (Frankenberg et al., 2005, 2006; Bergamaschi et al., 2009)) hot spots in methane concentrations have been seen around Lake Maracaibo from space (Frankenberg et al., 2011), but multiple years of data needed to be averaged to clearly see such a signal. Several global inverse studies have estimated Venezuelan emissions using multiple years of Greenhouse Gases Observing Satellite (GOSAT) (Schepers et al., 2012; Kuze et al., 2016) data and generally found higher emissions than predicted by bottom-up emission inventories. These "top-down" results tend to come with large uncertainty ranges on Venezuelan results due to a limited number of observations in the area or sensitivity of the inversion to underlying assumptions (Maasackers et al., 2019). Lu et al. (2021) found opposing corrections to mean 2010-2017 bottom-up Venezuelan emissions from inversions of in-situ (lower emissions) and GOSAT (higher emissions) data, as well as a small negative 2010-2017 trend over the Lake Maracaibo area from both. Worden et al. (2022) used 2019 GOSAT data in an inversion to report natural and anthropogenic Venezuelan emissions of 9.7 ± 1.3 and $8.6 \pm (0.9-1.5)$ Tg a⁻¹, respectively, about twice larger than the (UNFCCC-consistent)

55

bottom-up inventories they use as prior estimate. In an evaluation of several inverse studies, Scarpelli et al. (2022) proposed that venting and flaring of associated gas during oil production most likely explains the large differences between inventories and observation-based results.

60

The TROPOMI instrument was launched aboard ESA's Sentinel-5P satellite in 2017 and observes methane using its absorption features in the 2305–2385 nm shortwave infrared (SWIR) and the (757–774 nm) near-infrared (NIR) band. TROPOMI's 2600-km swath provides daily global coverage of total column methane at ~13:30 local time with a resolution of 7 km × 5.5 km at nadir (7 km × 7 km before August 2019)(Veeffkind et al., 2012; Lorente et al., 2021). 2019 TROPOMI data have
65 been used in a global inversion by Qu et al. (2021) to find upward corrections over Venezuela with respect to the bottom-up Scarpelli et al. (2020) inventory that estimated UNFCCC-consistent emissions for 2016. Their inversion just using TROPOMI data shows uniform upward correction to bottom-up emissions in Venezuela. When exclusively using or adding GOSAT data, some downward corrections compared to the bottom-up emissions around Lake Maracaibo appear. Yu et al. (2023) used 2018-
70 2019 TROPOMI data to find Venezuelan fossil fuel emissions of 4.8 (3.8–5.3) Tg a⁻¹, about 30% higher than the Scarpelli et al. (2020) prior value. The global daily coverage of TROPOMI can also be used to detect individual large methane plumes from “super-emitters”. Schuit et al. (2023) found one super-emitter methane plume near Lake Maracaibo in 2021 TROPOMI data using a machine learning approach. The number of such detections is most likely limited by the lack of coverage over the area.

75 We use the TROPOMI data to study Venezuela and the Lake Maracaibo area in more detail, including over recent years during which Venezuela's oil production steeply declined. We use 2018-2020 TROPOMI methane data in two inverse analyses at the regional and country level to estimate methane emissions in Venezuela and in particular the oil production region around Lake Maracaibo.

80 **2 Data & Methodology**

We use 2018-2020 TROPOMI methane data combined with two atmospheric transport models to estimate national and regional Venezuelan methane emissions. We utilize the v1.0 of the Integrated Methane Inversion framework (IMI (Varon et al., 2022)) to evaluate 2019 emissions for the entire country and use WRF-Chem (the Weather Research and Forecasting model (Skamarock et al., 2019)) to zoom in on the Lake Maracaibo hot spot area and estimate annual emissions for 2018, 2019, and
85 2020. Additionally, we contextualize the TROPOMI evaluation with methane observations from SCIAMACHY (SCanning Imaging Absorption SpectroMeter for Atmospheric CHartography) and GOSAT (Greenhouse Gases Observing Satellite) and flaring data from the VIIRS instruments (Visible Infrared Imaging Radiometer Suite (Elvidge et al., 2013; Colorado School of Mines Earth Observation Group, 2020)).



90 2.1 TROPOMI Satellite data

We use TROPOMI data from the SRON Scientific Product version 19_446 (Operational version 02.04.00) (Lorente et al., 2023) that uses a full-physics retrieval approach that simultaneously retrieves methane concentrations and the atmosphere's physical scattering properties. Lorente et al. (2023) improved upon previous TROPOMI methane retrievals by representing the retrieval's spectral dependence of the Lambertian surface albedo by a third-order instead of a second-order polynomial, 95 reducing the occurrence of artificial methane enhancements induced by spectral surface features (Barré et al., 2021). The retrieval shows good agreement with the Total Carbon Column Observing Network (TCCON) (Wunch et al., 2011) with an average bias of -0.3% (-5.3 ppb) and a station-to-station variability of 0.3% (5.1 ppb). The combination of persistent cloud cover, proximity to water and complicated topography make Venezuela as a whole, and the Lake Maracaibo area especially, a difficult area to observe from space. Based on this specific area and expert judgement, we therefore use data beyond the 100 regular data quality (Qa) = 1 recommended filter to optimize the number of observations over the region of interest while also filtering more anomalous data over the low albedo Amazon region. We used data over land with Qa values above 0.4; NIR Aerosol optical depth under 0.3; SWIR Aerosol optical depth under 0.1; SWIR albedo above 0.05; and cloud fractions under 0.015. For 2019, this set of filters gives us a total of 33485 observations over all of Venezuela and 4251 around Lake Maracaibo (8.3-11.1 °N, 72.7-69.9 °S). For 2018 and 2020, we find 2975 and 4976 observations over the Lake Maracaibo area. The 105 change in the number of annual observations is caused by the decreased along-track pixel size starting in August 2019 and the fact that for part of 2018, the instrument was in calibration mode and not producing daily observations. Compared to the IMI and WRF-Chem simulations, the relaxed filter increases the standard deviation of the prior model - observation mismatch by 3-4%. We perform a sensitivity inversion using the $Qa = 1$ data filtering to include this in our reported uncertainty (Section 2.4).

110 2.2 National model: Integrated Methane Inversion

We use the Integrated Methane Inversion (IMI (Varon et al., 2022)), which provides an analytical inversion framework using GEOS-Chem 13.4.0 as its transport model (<http://geos-chem.org>). The GEOS-Chem forward model runs are simulated on a $0.25^\circ \times 0.3125^\circ$ grid encompassing all of Venezuela, driven by GEOS Fast Processing (GEOS-FP) meteorological data from the NASA Global Modelling and Assimilation Office (Molod et al., 2012). We use the standard v2023-04 3-hourly IMI bound- 115 ary and initial conditions based on monthly 10-degree smoothing of TROPOMI values over land and latitudinal averages over water (Shen et al., 2021; Varon et al., 2022), but optimize these in the inversion. Methane has a long atmospheric lifetime compared to its residence time in our IMI simulation but nevertheless the IMI includes sinks of methane from oxidation by OH and Cl, stratospheric loss (Maasakkers et al., 2019), and soil uptake (Murguia-Flores et al., 2018). These sinks are not optimized in the inversion. We run the IMI forward model for 2019 over the domain shown in Figure 1b (-4.3°S - 17.5 °N, 78.4-54.7 °S, 120 encompassing Venezuela), using December 2018 as “spinup” to initialize the model's concentration field. We adapt the IMI framework to use the TROPOMI Science Product with our custom filtering (Section 2.1) and our ensemble inversion approach



including log-normal error distributions (Section 2.4).

2.3 Regional model: Weather Research and Forecasting model

125 To analyze emissions around Lake Maracaibo at higher resolution, we use the Weather Research and Forecasting (WRF-Chem)
model version 4.1 (Powers et al., 2017; Skamarock et al., 2019). We perform simulations for 2018, 2019, and 2020, using De-
cember of the year prior as a spinup. As shown in Figure 1c, the simulations were performed using three nested domains with
27, 9, and 3 km resolution, as they move in towards the Lake Maracaibo region. The outer two domains consist of 99×99
grid cells and the innermost domain has a 105×105 grid. The meteorology is driven by National Centre for Environmental
130 Prediction (NCEP) data (National Centre for Environmental Prediction, 2000) with the ‘tropical’ physics suite. We use the
Copernicus Atmosphere Monitoring Service (CAMS) global forecast at $0.4^\circ \times 0.4^\circ$ and 6-hr resolution to provide initial and
boundary conditions (Koffi and Bergamaschi, 2018), which we also optimize in the inversion. We subtract the soil sink from
the IMI from the WRF emissions but the effect is small (0.02 Tg a^{-1}).

135 2.4 Inverse Methodology

We estimate both national and regional emissions using Bayesian analytical inversion (Jacob et al., 2016) where we find the
optimal posterior solution ($\hat{\mathbf{x}}$) for the state vector (\mathbf{x}) as:

$$\hat{\mathbf{x}} = \mathbf{x}_A + \mathbf{S}_A \mathbf{K}^T \left(\mathbf{K} \mathbf{S}_A \mathbf{K}^T + \frac{\mathbf{S}_O}{\gamma} \right)^{-1} (\mathbf{y} - \mathbf{K} \mathbf{x}_A) \quad (1)$$

Where \mathbf{x}_A gives the prior state vector, \mathbf{S}_A the prior error covariance matrix, \mathbf{K} the Jacobian matrix representing the forward
140 model, \mathbf{S}_O the observational error covariance matrix, γ a regularization factor to prevent overfitting, and \mathbf{y} the observations.
The posterior emissions can be evaluated using the posterior error covariance matrix $\hat{\mathbf{S}}$ (Equation 2) and averaging kernel \mathbf{A}
(Equation 3, where \mathbf{I} is the identity matrix) that quantifies the extent the posterior emissions are informed by the observations.

$$\hat{\mathbf{S}} = (\gamma \mathbf{K}^T \mathbf{S}_O^{-1} \mathbf{K} + \mathbf{S}_A^{-1})^{-1} \quad (2)$$

$$145 \mathbf{A} = \mathbf{I} - \hat{\mathbf{S}} \mathbf{S}_A^{-1} \quad (3)$$

For the national analysis, we use perturbation sensitivity simulations with the IMI (sampled using TROPOMI averaging ker-
nels) to construct \mathbf{K} and estimate the impact of emissions on concentrations observed by TROPOMI, including offshore emis-
sions. As TROPOMI does not provide enough information to individually optimize emissions from every grid cell and running
the associated sensitivity simulations for every grid cell would be computationally infeasible, we construct the state vector



150 by grouping grid cells together using k-means clustering. Since most emissions are located in the northern half of Venezuela
(Figure 1a), we use the highest density of clusters (124) there. We use an additional 24 elements for the southern part of the
country, and another 50 in a 5 degrees buffer zone around the country. The buffer zone elements mainly serve to correct the
background concentrations of air floating into Venezuela. We add three elements to optimize offshore emissions in Lake Mara-
caibo and off the northeastern coast of Venezuela. We also incorporate a state vector element to capture the sensitivity to the
155 background by scaling the boundary conditions, giving 202 state vector elements in total (or 213 when scaling the boundary
conditions monthly).

For the three annual WRF inversions, we simulate individual tracers for each state vector element (different parts of the do-
main) to include them in the state vectors. We divide the inner domain into a 6×6 grid ($\sim 50 \text{ km} \times 50 \text{ km}$) to have a high
160 resolution over the area of interest. We divide the outer and middle domains in 8×8 grids excluding the parts covered by the
inner domain(s) and aggregate elements in the northwest and northeast corners of the outer domain, which are mostly covered
by water. We use the state vector elements in the outer domains as "buffer" elements similar to the IMI. Finally, our 74-member
state vector is completed with 12 elements scaling the monthly CAMS-based background. We also perform an inversion where
we combine these last 12 elements into one annual background correction.

165 Our prior bottom-up emissions are shown in Figure 1a. We use 2019 oil, gas, and coal emissions from the Global Fuel Ex-
ploitation Inventory (GFEI v2 (Scarpelli et al., 2022)) for all years. The remaining anthropogenic emissions, most prominently
including livestock and waste management, are 2018 emissions from the Emissions Database for Global Atmospheric Re-
search (EDGAR) v6 (Crippa et al., 2021). The recent EDGAR v7 inventory (Crippa et al., 2022; Commission et al., 2021)
170 estimates that Venezuelan livestock and waste management emissions have changed by less than 5% from 2018 to 2020. Nat-
ural emissions from wetlands come from WetCHARTs v1.2.1 (Bloom et al., 2017), and we included IMI-standard emissions
from termites and geological seeps (Varon et al., 2022) as well as fire emissions from the Global Fire Emissions Database
(GFED) v4 (Randerson et al., 2018). Emission maps per source sector are included in Table 1 and Supplemental Figure A1.

175 When comparing to TROPOMI for the inversion, we aggregate observations on a 0.2° grid to reduce the influence of small-scale
transport errors (Maasakkers et al., 2022). We use an observational error of 15-19 ppb based on the standard deviation of the
prior model - observation mismatch. To analyze the sensitivity of our inversions and estimate their uncertainties, we construct
an ensemble of inversions varying inputs (e.g., scaling prior emissions), assumptions (e.g., varying the error distribution), and
settings (e.g., varying the regularization). To generate our ensemble we: (1) use prior emissions with a uniform scaling of 70,
180 100 and 130% of prior emissions, (2) use observations over just the Lake Maracaibo area or the entire (IMI or WRF) model
domain, (3) aggregate observations over resolutions of 0.1° , 0.2° , and 0.5° , (4) based on L-curve analysis we find an optimal
regularization factor of $\gamma = 0.25$ (Hansen, 1999) and include inversions with $\gamma = 0.1$ and $\gamma = 0.5$ as well, (5) use normal or
log-normal errors following Maasakkers et al. (2019), (6) use the TROPOMI filters with the filtering described in Section
2.1 or $Qa = 1$ filtering, (7) optimize the boundary conditions on a monthly or annual basis, (8) use the TROPOMI data with

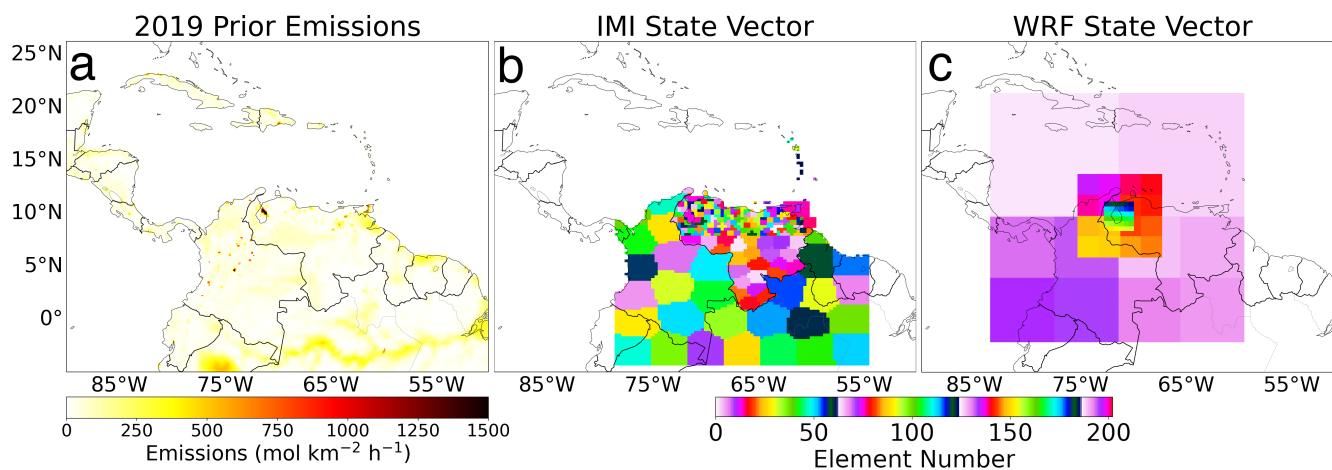


Figure 1. Prior emissions used in the inversion (a) and state vector elements used in the IMI (b) and WRF (c) inverse analyses. The different WRF domains can be discerned based on the resolution of the state vector elements.

185 and without the standard albedo correction, and (9) when aggregating n observations we assume that errors on aggregated observations scale with the central limit theorem ($\sim \sqrt{n}$) or do not decrease. We report the means and conservative uncertainty ranges based on standard deviations of the resulting 1728-member ensembles for the IMI and WRF analyses.

2.5 Supporting satellite data

We use data from three satellite instruments to provide context on the TROPOMI-based results. The SCIAMACHY instrument aboard ENVironmental SATellite (ENVISAT), was the first satellite instrument to provide global coverage total column methane data (Frankenberg et al., 2005, 2006). Operational between 2003 and 2012, it had a resolution of 30 km × 60 km. Observations after 2005 are of lower quality because of detector degradation (Kleipool et al., 2007). SCIAMACHY uses the 1.65 μm absorption band of methane, which allows the use of co-retrieved CO₂ in the proxy method. In that method, the observed ratio of methane to CO₂ is multiplied with a prior (modeled) CO₂ column to estimate total column methane, making the retrieval less sensitive to artefacts and atmospheric scattering. We use the proxy retrieval data of Frankenberg et al. (2011).

The GOSAT satellite was launched in 2009 and observes methane total column mixing ratios using its TANSO-FTS instrument (Butz et al., 2011; Schepers et al., 2012; Kuze et al., 2016). In its default mode, GOSAT observes circular pixels of 10.5 km diameter, separated by ~250 km, at 13:00 local time. The observation track is repeated every three days while a target mode can be used to observe additional locations. Like SCIAMACHY, GOSAT uses the 1.65 μm absorption band that is used in both full-physics and proxy retrievals. We use the University of Leicester v9.0 proxy product (Parker and Boesch, 07 May 2020). Data from its successor, GOSAT-2 is available starting February 2019 (Suto et al., 2021). We use GOSAT(-1) here to have



uniform data across the studied time period.

205 The Suomi National Polar-Orbiting Partnership (SNPP) and NOAA-20 (J01) satellites both carry a VIIRS (Visible Infrared
Imaging Radiometer Suite) multispectral imager that can be used to detect radiant emissions from gas flares in the 1.6 μm
band at 750-m spatial resolution (Elvidge et al., 2013). These observed heat radiances can be converted to flared gas volumes
using the Stefan–Boltzmann law and a calibration based on reported volumes of flared gas (Elvidge et al., 2016). This approach
has been calibrated and used at both the field and well-level (Zhang et al., 2020; Maasakkers et al., 2022). Here we use the
210 NightFire v3.0 product (Colorado School of Mines Earth Observation Group, 2020) together with the well-level calibration
from Maasakkers et al. (2022), who assume a methane content of 95%, to estimate the amount of gas/methane flared at sites in
the Lake Maracaibo region.

3 Results and Discussion

215 Figure 2 compares the coverage of SCIAMACHY for 2003-2010 (Panel a) with TROPOMI (b) and GOSAT (c) for 2019. The
figure shows the vast improvement provided by TROPOMI in terms of precision compared to SCIAMACHY (where even
the multi-year average contains very noisy observations) and in terms of coverage compared to GOSAT. Some areas lack
TROPOMI coverage because of steep elevation gradients such as in the Andes or prohibitively low albedo values such as over
the Amazon. Total column values are lower over areas with higher elevation where the low-concentration stratosphere has a
220 larger relative impact on the column-averaged values. Some areas (eastern Colombia, Amazon) show some albedo-induced
high and low methane values that are based on only a few observations. Enhanced methane values are seen around Lake
Maracaibo in western Venezuela with all instruments, with especially the eastern coast of the lake standing out in TROPOMI.
In annual GOSAT data (Supplemental Figure A2), persistent enhancements can be seen around the lake between 2010 and
2020 but the limited spatial coverage makes it hard to attribute these enhancements to underlying emissions. About 20 days
225 of TROPOMI data in 2019 have been manually identified as having plume-like signals originating from the lake area, even
though the combination of persistent cloud cover, proximity to water, and complicated topography makes seeing fully devel-
oped plumes impossible. Figure 2d shows Venezuelan facility-level flared gas volumes estimated based on 2019 VIIRS data.
Clusters of flares can be seen both on and along Lake Maracaibo as well as in the Orinoco basin in the eastern part of the
country, matching the distribution of oil production emissions (Supplemental Figure A1).

230

Compared to TROPOMI our 2019 IMI-based inversion improves our simulation’s mean absolute bias from 15 to 12 ppb and
increases the correlation between model and observations from $r = 0.47$ to 0.53 (Supplemental Figure A1a,b). We find an
annual average correction of the background, represented by the IMI boundary and initial conditions, of 0.3%. Figure 3 shows
the results for the 2019 IMI-based inversion over Venezuela. The prior estimate for Venezuela totals 6.6 Tg a^{-1} , and the
235 ensemble-mean posterior is 7.5 Tg a^{-1} with an ensemble standard deviation of 1.8 Tg a^{-1} . Figure 3a and 3b show emissions

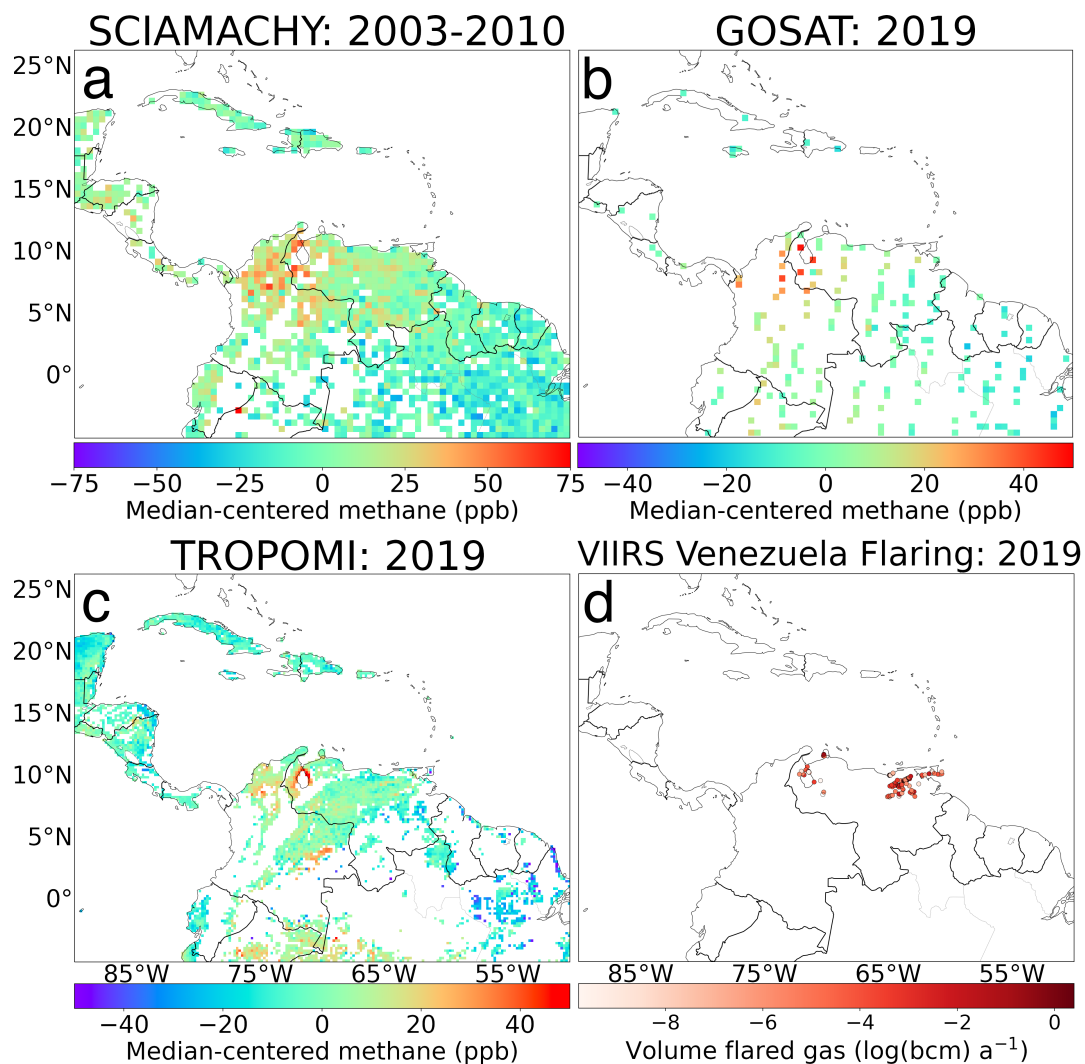


Figure 2. Average methane enhancements over northern South America from SCIAMACHY for 2003-2010 (a), GOSAT for 2019 (b), and TROPOMI for 2019 (c). The median values of the individual images have been subtracted to obtain median-centered enhancements. SCIAMACHY and GOSAT are visualized on a 0.5° grid while TROPOMI is shown on a 0.2° grid. Only grid cells with at least five observations are shown. All panels have some saturated values. Panel d shows the facility-level amounts of gas flared based on radiant heat observed by VIIRS in 2019 in billion cubic meters of natural gas (bcm).

are scaled up over areas with the most emissions: Lake Maracaibo in the Northwest and the Orinoco Belt in the Northeast. Global studies interpreting satellite data with GEOS-Chem as the transport model also found upward corrections albeit using the higher Scarpelli et al. (2020) emissions as prior (Qu et al., 2021; Lu et al., 2021). Emissions in most of the low-emitting southern part of the country get scaled down slightly. However, the diagonal of the averaging kernel (Figure 3c) shows there is little information in the TROPOMI data for most of Venezuela, with the exception of the Lake Maracaibo emission hot spot.



Many of the highest averaging kernel values fall in the buffer cells outside Venezuela and especially the upward correction in the Orinoco basin is poorly informed by the satellite data. To estimate posterior sector-specific emissions (Figure 3d and Table 1), we multiply the scale factors of each state vector element by their prior sectoral emissions. The three major sources of methane in Venezuela are oil production, wetlands, and livestock. We find the largest relative correction for oil: 1.6 (0.8-2.4),
 245 in large part driven by the upward correction over Lake Maracaibo. Oil production is responsible for 24 (17-30)% of national emissions, up from 17% in the prior. Emissions from natural gas, fires, termites, and other sources all play very minor roles in both the prior and posterior emission totals. Also shown in Figure 3d are the fractions of the emissions with some constraint from TROPOMI (associated diagonal averaging kernel larger than 0.05, following Nesser et al. (2023)). We find that for both oil and wetland emissions a large fraction of emissions at the national level can not be constrained by the TROPOMI data.
 250 The associated spread in the inversion ensemble is mainly driven by the ensemble members that scale the prior as well as the number of observations used (for example due to the data filtering) and the weight attributed to them in the inversion with the regularization factor with some contribution from the albedo correction (Supplement Figure A4). Overall, this indicates that at the current stage, evaluating national total emissions from Venezuela with a single year of TROPOMI data is not feasible with meaningful uncertainty.

255

Table 1. 2019 prior and posterior emissions for Venezuela and Lake Maracaibo based on the IMI and WRF inversions of TROPOMI data in Tg a^{-1}

Source Sector	Venezuela		Lake Maracaibo ^b		
	Prior ^a	IMI Posterior ^c	Prior ^a	WRF Posterior ^c	IMI Posterior ^c
Wetlands	3.64	3.58 (2.79 – 4.37)	0.11	0.14 (0.08 – 0.20)	0.18 (0.10 – 0.26)
Livestock	1.11	1.24 (0.90 – 1.58)	0.28	0.32 (0.23 – 0.40)	0.34 (0.24 – 0.44)
Oil	1.10	1.77 (0.88 – 2.65)	0.79	0.64 (0.53 – 0.75)	1.25 (1.00 – 1.51)
Termites	0.14	0.13 (0.10 – 0.16)	0.01	0.01 (0.01 – 0.01)	0.01 (0.01 – 0.02)
Fires	0.13	0.13 (0.11 – 0.16)	0.01	0.01 (0.01 – 0.01)	0.01 (0.01 – 0.02)
Gas	0.02	0.03 (0.02 – 0.04)	0.00	0.00 (0.00 – 0.00)	0.00 (0.00 – 0.00)
Other	0.46	0.60 (0.21 – 1.00)	0.10	0.12 (0.08 – 0.17)	0.15 (0.12 – 0.18)
Total	6.60	7.48 (5.68 – 9.29)	1.3	1.24 (1.02 – 1.46)	1.95 (1.55 – 2.36)

^a Prior emissions include 2019 Oil, gas, and coal emissions from GFEI v2 (Scarpelli et al., 2022)), 2018 livestock and other anthropogenic emissions from EDGAR v6 (Crippa et al., 2021), wetland emissions from WetCHARTs v1.2.1 (Bloom et al., 2017), IMI-standard emissions from termites and geological seeps (Varon et al., 2022), and GFED v4 fire emissions (Randerson et al., 2018).

^b The Lake Maracaibo area encompasses 8.3-11.1 °N, 72.7-69.9 °S

^c We report ensemble means and standard deviations

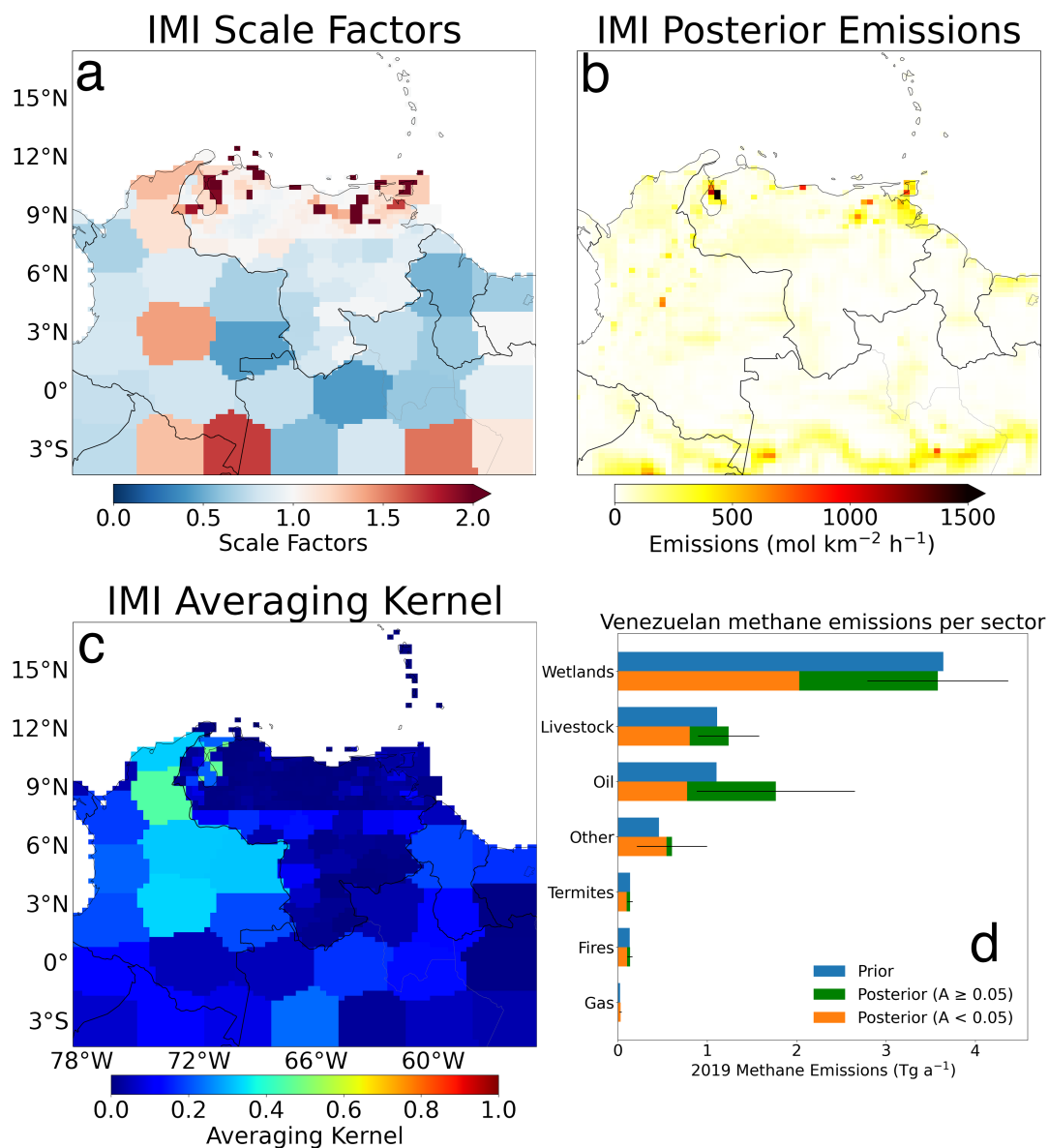


Figure 3. Inversion results from the 2019 IMI inversion over Venezuela with: (a) posterior:prior scaling factors, (b) posterior emissions, (c) averaging kernel sensitivities, and (d) nationally aggregated prior and posterior emissions per source sector, with the fraction of emissions constrained with averaging kernels (A) above 0.05 shown in green. Values shown are means of the inversion ensemble with the ranges showing the associated ensemble standard deviations.

Compared to TROPOMI, our 2019 WRF-based inversion improves the mean absolute bias over the Lake Maracaibo area from 57 to 12 ppb and increases the correlation between model and observations from $r = 0.42$ to 0.47 (Supplemental Figure A3c,d).



In the absence of sub-orbital observations, we use the proxy-method GOSAT (Figure 2b) data as the most independent data set to evaluate our inversion results. We find that the mean absolute bias with GOSAT decreases from 71 to 19 ppb, mostly due to the upward correction to the CAMS background of 3% on average with some remaining bias due to a mean offset between GOSAT and TROPOMI over the region. We find that correlation between model and GOSAT improves from $r = 0.56$ to $r = 0.58$, mainly due to corrections to emissions. Figure 4 shows the results of the WRF-based inversion over Lake Maracaibo, focusing on the results from the inner domain. Lake Maracaibo emissions are estimated at 1.2 (1.0 - 1.5) Tg a^{-1} (Supplement Figure A5), dominated by oil production (51 (44-58)% of total emissions) and lower than the results based on the IMI inversion, 2.0 (1.6 - 2.4) Tg a^{-1} (Source sector emission totals are included in Table 1). The averaging kernel sensitivities (Figure 4c) show that the area east of Lake Maracaibo is the only area where TROPOMI provides significant information. This is not unexpected as the large prior emissions there would have a large effect on the scarce TROPOMI observations over the area. This is also the main area where emissions are decreased with respect to the prior, with most of the remainder of the domain showing a slight increase but very small averaging kernels. As Figure 4d shows, the oil emissions are well characterized by the inversion as they are clustered in the area where TROPOMI provides most information with an uncertainty range including the prior value. While inefficient flaring can play a role, we find oil emissions that are larger than the annual mass of methane flared in the area (0.6 Tg in 2019 assuming a 95% methane content) based on VIIRS, suggesting the majority of emissions come from other sources such as leaks or vents. Emissions from the other source sectors (predominantly livestock and wetlands) show small increases that are insignificant compared to the prior and show relatively worse constraints from TROPOMI as a larger fraction of the emissions occurs outside of the well-constrained hot spot area.

To take advantage of the two independent model simulations and better understand the differences with the IMI inversion, we perform an additional WRF inversion (not included in the ensemble). Here, we resample the WRF simulation output to the IMI grid to perform a “most IMI-like” inversion and find Lake Maracaibo emissions of 1.4 Tg a^{-1} compared to 2.3 Tg a^{-1} when using equivalent inversion settings in the IMI framework. This resampling reduces the probability of plumes in WRF having large spatial mismatches with plumes seen in TROPOMI, which could lead to underestimation of the emissions. The remaining difference after aligning sampling suggests the underlying transport is the main culprit. There are other differences between the models, such as the representation of the background, loss processes, and the stratosphere but these are unlikely to have a major effect on the emission estimate for the concentrated hot spot area because of the damping influence of the optimizations of the background and “buffer” elements around the area. To further investigate the differences in transport, we compare the WRF output 10-m wind speed based on NCEP to the GEOS-FP 10-m wind (used in the IMI) over the lake (sampled at 9.8 N° , 71.5 S°). We find that at the overpass of TROPOMI ($\sim 18:00$ UTC), the GEOS-FP average wind speed of 2019 is $2.8 \pm 1.2 \text{ m s}^{-1}$ (standard deviation), a factor 1.9 larger than the NCEP-based wind of $1.5 \pm 0.8 \text{ m s}^{-1}$. The independent ERA5 reanalysis (Hersbach et al., 2020) gives a wind speed of $1.9 \pm 0.7 \text{ m s}^{-1}$ for the same time and location. Similarly, we find winds between 975 and 800 hPa in GEOS-FP are a factor 1.6 larger than in NCEP. The lower NCEP winds lead to a slower ventilation of the area in WRF and result in a build-up of methane. Therefore, the WRF inversion “requires” lower emissions to explain the same methane enhancement in TROPOMI than the IMI inversion that has a stronger wind speed in the area,

showing the importance of reliable meteorological data. As there are no observations or large emissions nearby (partly due to the proximity to the ocean), the transport-induced difference in emissions is not compensated for by nearby grid cells but instead carries through to the regional budget.

295

Figure 5 shows annual 2018-2020 regional emissions for the Lake Maracaibo region based on annual WRF inversions. Compared to GOSAT, mean bias over these three years improves from 73 to 23 ppb while correlation improves from $r = 0.49$ to $r = 0.53$. As the uncertainty ranges from the inversion ensemble overlap, a significant trend cannot be seen but both the temporal evolution of the base inversion as well as the other ensemble members suggest a decrease. This decrease would be consistent with the also shown 2018-2020 decreases in flaring activity observed by the VIIRS satellite instruments ($\sim 20\%$ drop), reported marketed oil production ($\sim 60\%$ drop (Rystad Energy, 2022)), and reported marketed gas production ($\sim 90\%$ drop, albeit absolute numbers are small (Rystad Energy, 2022)). Our decrease is close to the 30% decrease in 2018-2020 Venezuelan oil/gas emissions predicted by EDGAR v7. Even with the 2018-2020 drop in the base WRF inversion ($\sim 20\%$), our results suggest an increasing methane intensity because of the strongly reduced production. Following Schneising et al. (2020) we express the emissions as methane emission intensity to the energy content of the combined oil and gas production in the area. We find intensities of 11, 13, and 23% for 2018-2020, with a value of 21% for 2019 based on the IMI analysis. These values are much higher than intensities of 1-4% Schneising et al. (2020) found for production regions in the US and Turkmenistan. The increasing methane emission intensity trend points at emissions that are independent of the amount of oil and gas production and likely related to the neglected or abandoned infrastructure in the region.

300

305

310

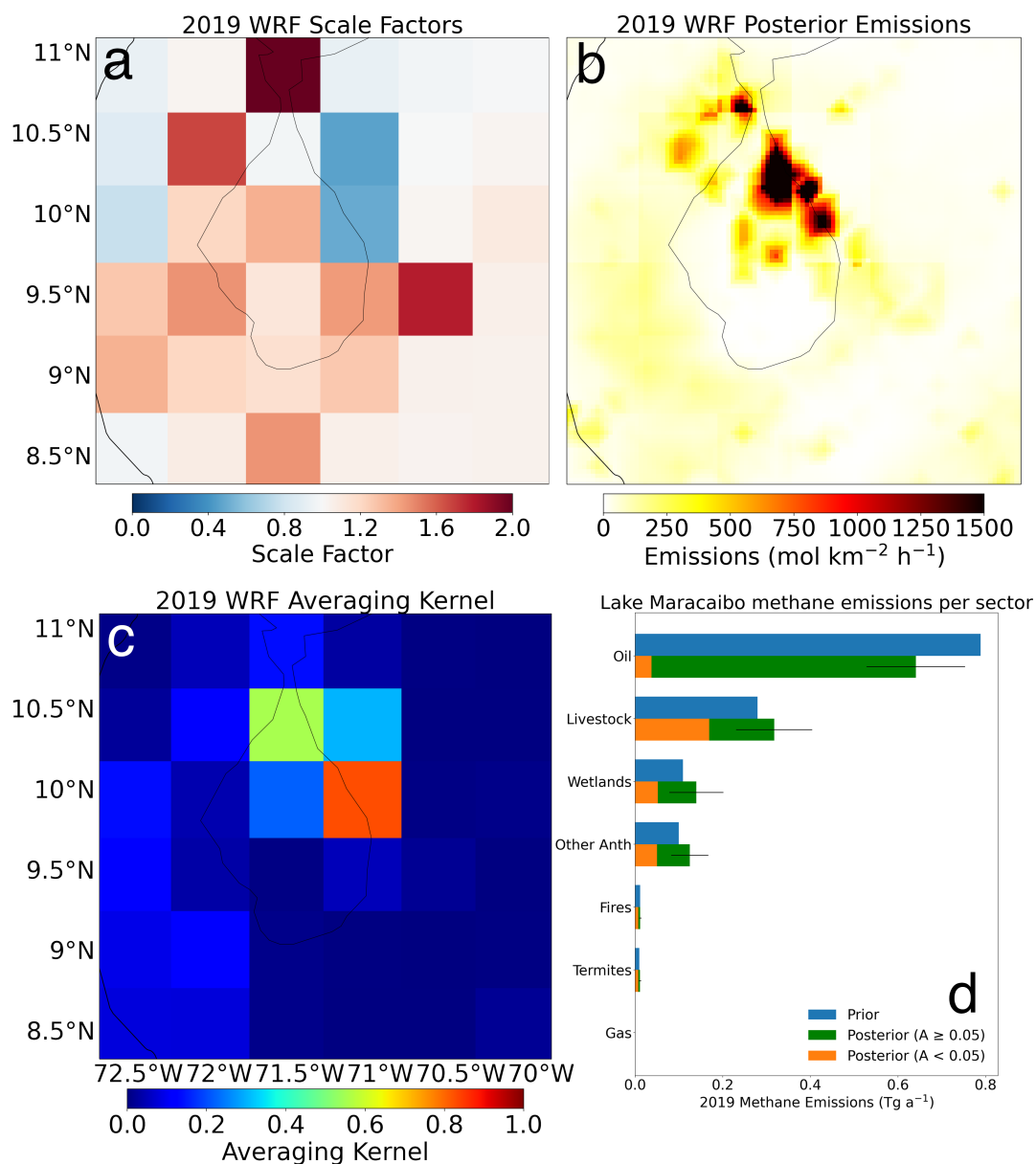


Figure 4. Inversion results from the 2019 WRF inversion over Lake Maracaibo with: (a) posterior:prior scaling factors, (b) posterior emissions, (c) averaging kernel sensitivities, (d) aggregated prior and posterior emissions per source sector sector, with the fraction of emissions constrained with averaging kernels (A) above 0.05 shown in green. Values shown are means of the inversion ensemble with the ranges showing the associated ensemble standard deviations.

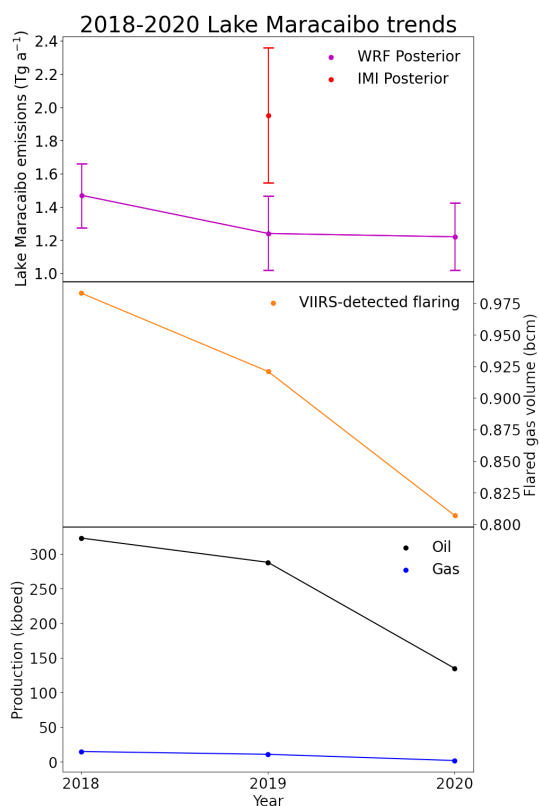


Figure 5. Annual results from the 2018-2020 inversions, suggesting a downward trend in emissions over the region. Also shown are VIIRS-observed flared volumes of natural gas and reported oil and gas production for the same domain (Rystad Energy, 2022), all showing decreases from 2018 to 2020.



4 Conclusions

We performed analytical inversions with 2018-2020 TROPOMI satellite methane data using two different models to estimate methane emissions over Venezuela with a focus on emissions from the oil production area around Lake Maracaibo that has long been identified as a methane hot spot. TROPOMI provides unprecedented daily global coverage at city-scale resolution showing a clear hot spot around the eastern shore of the Lake but the area remains difficult to observe due to elevation, low surface albedo, and persistent cloud cover.

Our national analysis using the IMI framework shows 2019 emissions are a factor 1.1 (0.9-1.4) higher than predicted by bottom-up inventories, with emissions from oil production showing the largest relative correction of factor 1.6 (0.8-2.4). TROPOMI can provide limited information on Venezuelan emissions because the number of observations in the area is limited by elevation gradients, persistent cloud cover, and low surface albedo. Based on the averaging kernel of the (TROPOMI) inversion, the satellite data cannot constrain about half of posterior national emissions of 7.5 (5.7-9.3) Tg a⁻¹. Especially emissions over the eastern Orinoco production basin show little TROPOMI sensitivity, while the inversion does show sensitivity to the Lake Maracaibo area.

Our focused analysis of the Lake Maracaibo region using WRF shows that the 2019 emissions in the area of 1.2 (1.0 - 1.5) Tg a⁻¹, predominantly from oil production, are well constrained by TROPOMI and consistent with bottom-up inventories but lower than the regional IMI results. We find the difference with the IMI is due to the stronger winds in the GEOS-FP meteorology driving the IMI compared to the NCEP winds used in WRF. Analyzing 2018-2020 annual emissions over Lake Maracaibo, we find a decrease in emissions of ~20% that is within the uncertainty margin of our ensemble, that together with strongly decreased local oil/gas production leads to a more than doubling of the implied methane emission intensity (11 to 23%) expressed against combined oil and gas production, much higher than previous studies have found for other oil/gas production regions around the globe. Our work provides better insight in Venezuelan emissions but also improves our understanding of the capabilities of using satellite data and (inverse) models at different scales. Our work can be used to target future analysis including extending our analysis for later years and incorporating facility-scale methane observations from high-spatial-resolution satellites and suborbital observations to give additional insight in the (evolution of) local emissions from different source sectors and serve as an independent verification of satellite-based inversion results.

Code availability. The IMI codes are available at <https://imi.seas.harvard.edu>. The WRF-Chem model code is available at <https://ruc.noaa.gov/wrf/wrf-chem/>.



Data availability. The TROPOMI data are available at ftp.sron.nl/open-access-data-2/TROPOMI/tropomi/ch4/19_446/. The GOSAT data used can be accessed at <https://dx.doi.org/10.5285/18ef8247f52a4cb6a14013f8235cc1eb>. VIIRS NightFire V3.0 radiant heat data are available on https://eogdata.mines.edu/download_viirs_fire.html. The IMI input data: GEOS-FP meteorology, emission fields, boundary conditions fields, and meteorological fields are available at <https://registry.opendata.aws/geoschem-input-data>. The NCEP 6-hourly meteorology are available at <https://rda.ucar.edu/datasets/ds094.0/>. The CAMS boundary conditions can be obtained from <https://apps.ecmwf.int/datasets/data/cams-nrealtime/levtype=pl/>.

Author contributions. BN, JDM, and IA developed the conceptual ideas for the study. BN performed the analysis with input from SN and JDM. RG and MO provided the production analysis and supported the contextualization of the project. DJV and MPS supported the IMI analysis. AL and TB provided the TROPOMI data and associated support. RJP provided support on the GOSAT data. BN and JDM wrote the manuscript with inputs from all co-authors.

Competing interests. At least one of the (co-)authors is a member of the editorial board of Atmospheric Chemistry and Physics.

Acknowledgements. The authors thank the team that realized the TROPOMI instrument and its data products, consisting of the partnership between Airbus Defence and Space Netherlands, KNMI, SRON, and TNO, commissioned by NSO and ESA. Sentinel-5 Precursor is part of the EU Copernicus program, Copernicus (modified) Sentinel-5P data (2018-2020) have been used. Part of this work was carried out on the Dutch national e-infrastructure, we thank SURF (www.surf.nl) for the support in using the National Supercomputer Snellius. BN and SN acknowledge funding through the UNEP CCAC Methane Studies and the Environmental Defense Fund (EDF). AL and TB acknowledge funding through the TROPOMI national program through NSO. RJP is funded via the UK National Centre for Earth Observation (Grant: NE/W004895/1). This research used the ALICE high-performance computing facility at the University of Leicester for the GOSAT retrievals and analysis. We thank the Japanese Aerospace Exploration Agency, National Institute for Environmental Studies and the Ministry of Environment for the GOSAT data and their continuous support as part of the Joint Research Agreement. We thank Hartmut Bösch for his contribution to the University of Leicester GOSAT product.



Appendix A: Supplemental figures

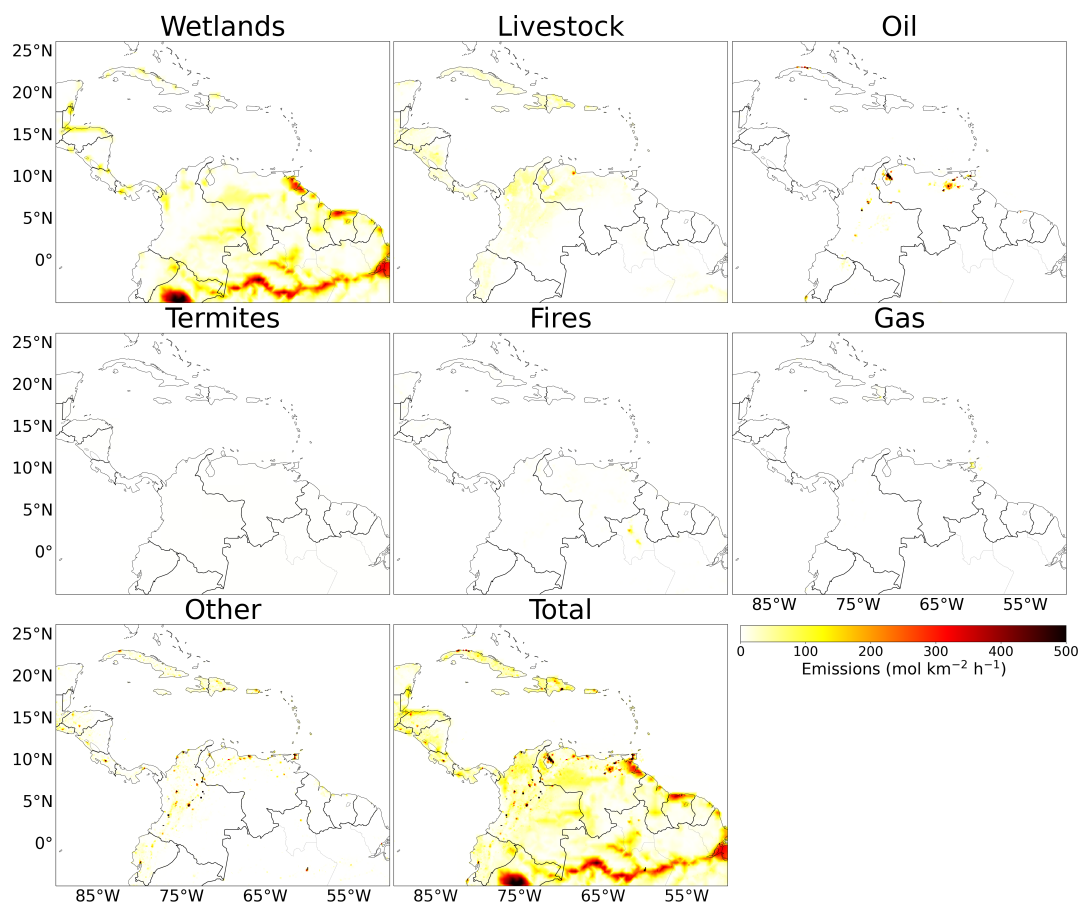


Figure A1. 2019 Prior emissions by source sector as described in Table 1.

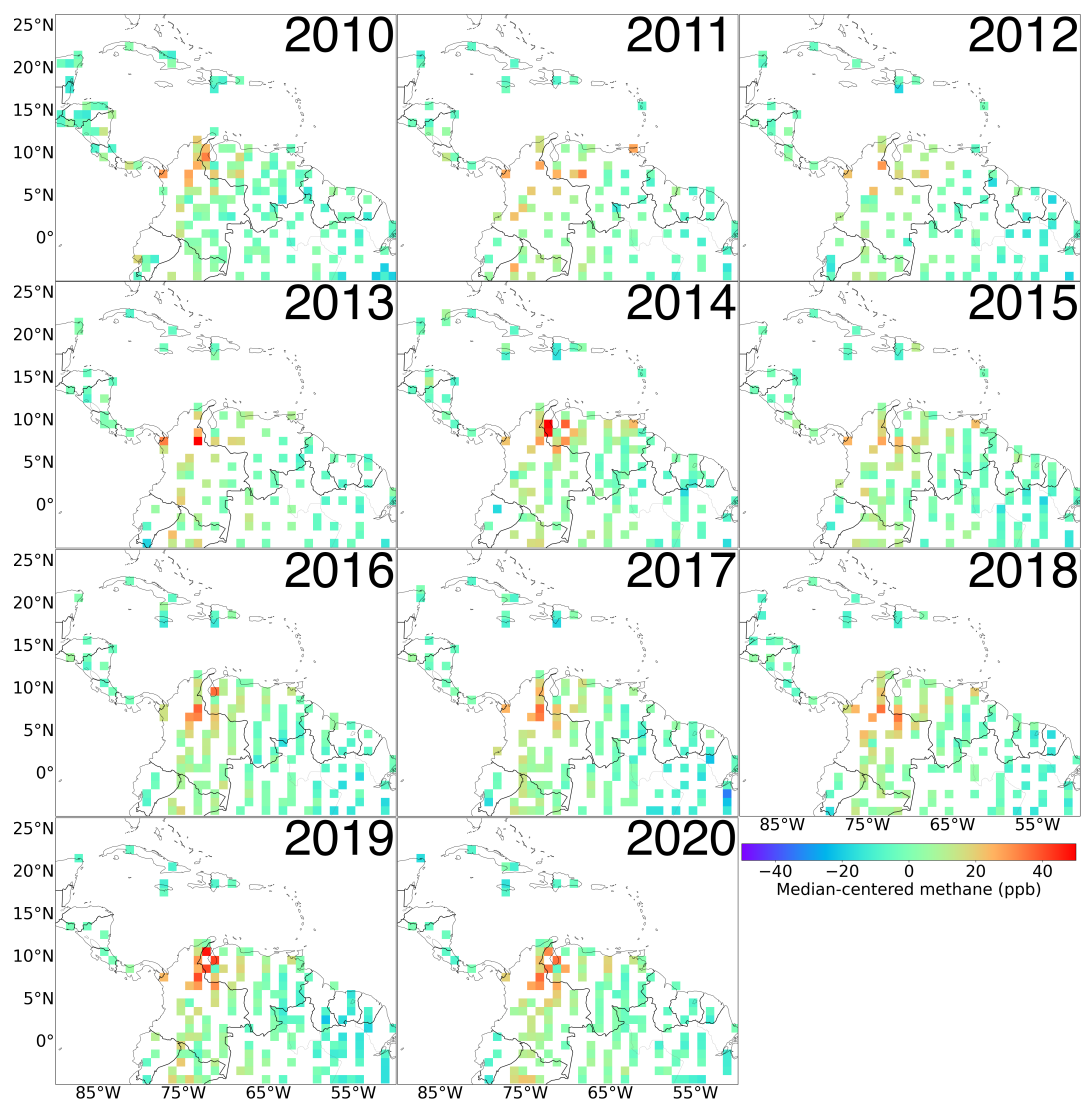


Figure A2. Annual average methane enhancements over northern South America from GOSAT for 2010–2020 on a 0.5° grid. The median values of the individual images have been subtracted to obtain median-centered enhancements. Only grid cells with at least five observations are shown. All panels have some saturated values.

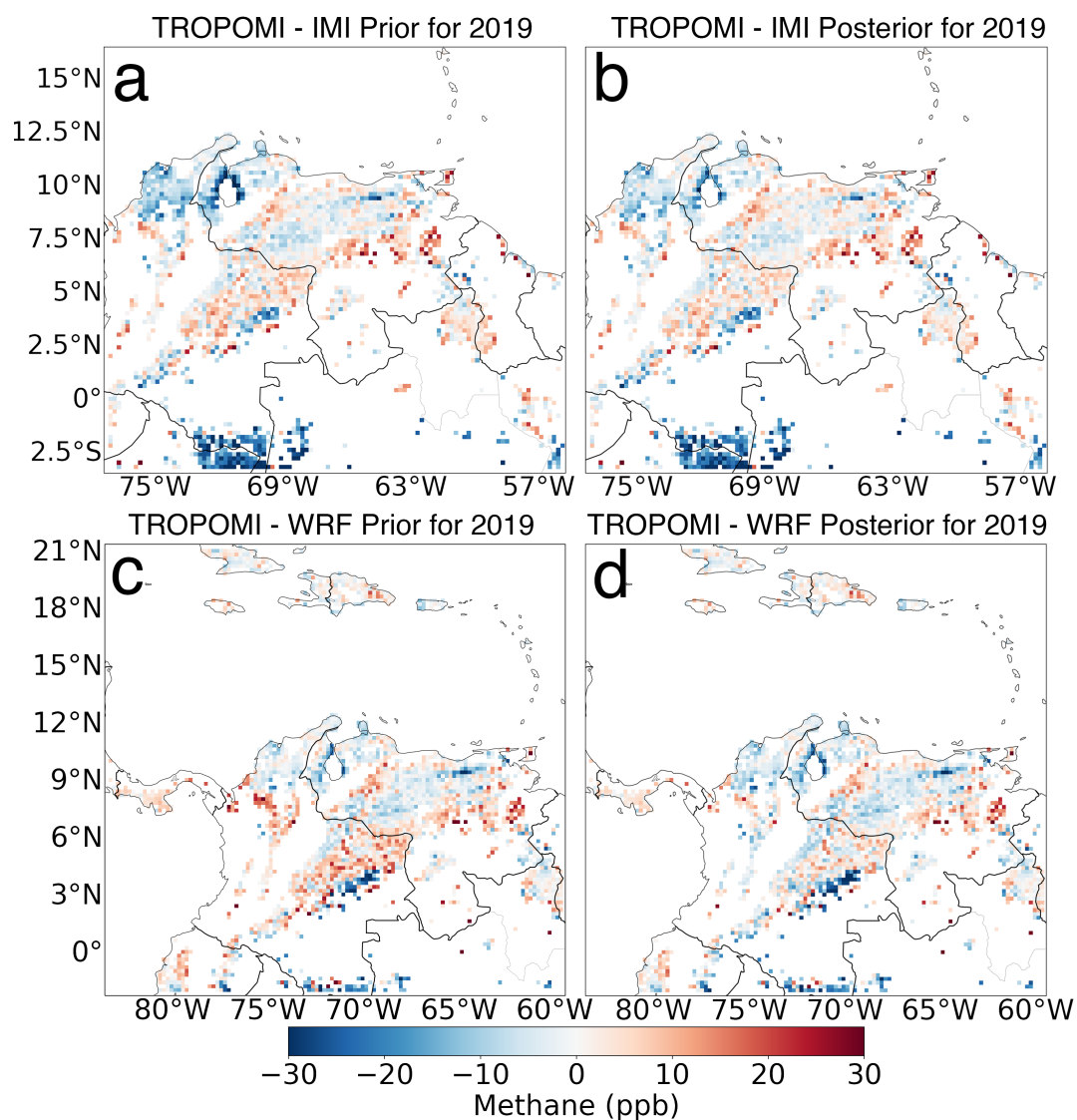


Figure A3. 2019 differences between TROPOMI and the IMI (a,b) and WRF (c,d) prior and posterior simulations. Only grid cells with at least five observations are shown. Prior panels already include the corrections to the background from the inversions to isolate the influence of corrections to emissions. Changes between the prior and posterior are small visually as averages only depend on a few (sometimes uncertain) observations, not all differences are attributable to emissions, and the state vectors have very limited resolution over much of the domain. The inversions cover slightly different domains as shown in Figure 1.

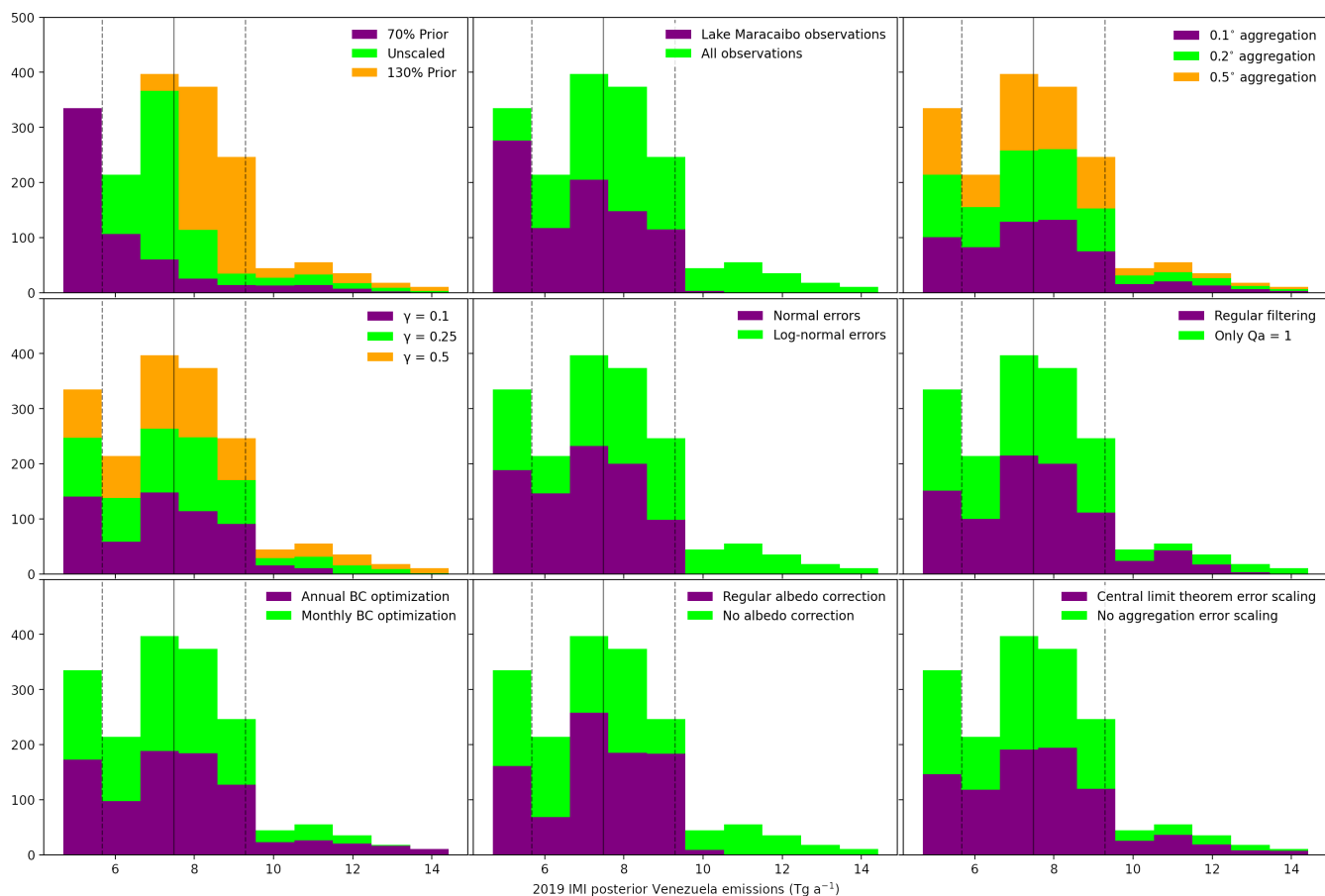


Figure A4. Histograms showing total Venezuelan emissions from the IMI inversion ensemble for 2019. Individual panels show the effect of the different ensemble characteristics described in Section 2.4. The solid line shows the ensemble mean (7.48 Tg a^{-1}) and the dashed lines show the associated standard deviation ($\pm 1.81 \text{ Tg a}^{-1}$).

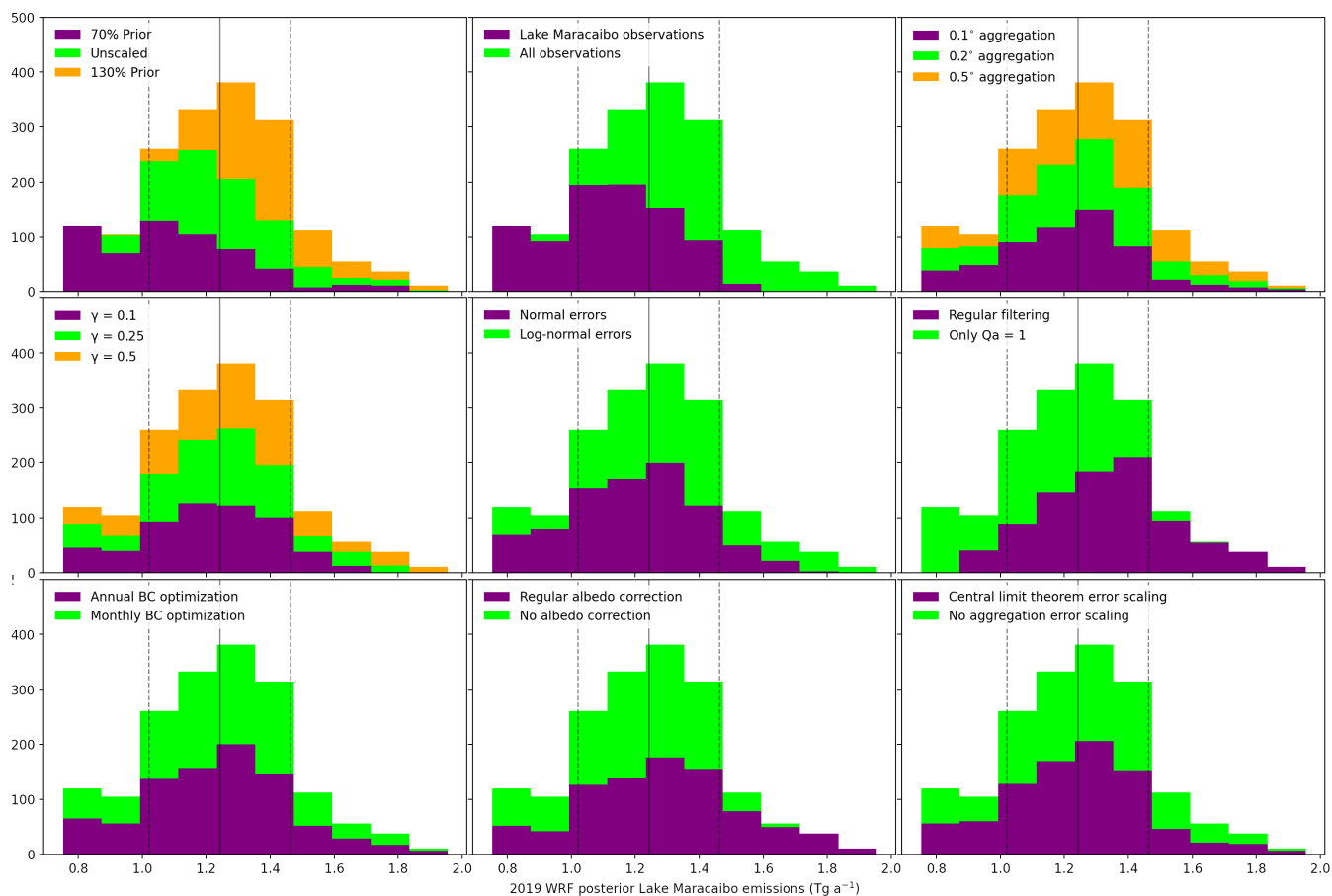


Figure A5. Histograms showing Lake Maracaibo emissions from the WRF inversion ensemble for 2019. Individual panels show the effect of the different ensemble characteristics described in Section 2.4. The solid line shows the ensemble mean (1.24 Tg a^{-1}) and the dashed lines show the associated standard deviation ($\pm 0.22 \text{ Tg a}^{-1}$).



References

- 365 AP News: Fishermen live in stain of Venezuela's broken oil industry, Article by Scott Smith, available at: <https://apnews.com/article/caribbean-ap-top-news-venezuela-international-news-environment-2cd2a3b985a4402e820049053aee473c>, 2019.
- Barré, J., Aben, I., Agustí-Panareda, A., Balsamo, G., Bousserez, N., Dueben, P., Engelen, R., Inness, A., Lorente, A., McNorton, J., Peuch, V.-H., Radnoti, G., and Ribas, R.: Systematic detection of local CH₄ anomalies by combining satellite measurements with high-resolution forecasts, *Atmospheric Chemistry and Physics*, 21, 5117–5136, <https://doi.org/10.5194/acp-21-5117-2021>, 2021.
- 370 Bergamaschi, P., Frankenberg, C., Meirink, J. F., Krol, M., Dentener, F., Wagner, T., Platt, U., Kaplan, J. O., Körner, S., Heimann, M., et al.: Satellite cartography of atmospheric methane from SCIAMACHY on board ENVISAT: 2. Evaluation based on inverse model simulations, *Journal of Geophysical Research: Atmospheres*, 112, 2007.
- Bergamaschi, P., Frankenberg, C., Meirink, J. F., Krol, M., Villani, M. G., Houweling, S., Dentener, F., Dlugokencky, E. J., Miller, J. B., Gatti, L. V., et al.: Inverse modeling of global and regional CH₄ emissions using SCIAMACHY satellite retrievals, *Journal of Geophysical*
375 *Research: Atmospheres*, 114, 2009.
- Bloom, A. A., Bowman, K. W., Lee, M., Turner, A. J., Schroeder, R., Worden, J. R., Weidner, R., McDonald, K. C., and Jacob, D. J.: A global wetland methane emissions and uncertainty dataset for atmospheric chemical transport models (WetCHARTs version 1.0), *Geoscientific Model Development*, 10, 2141, 2017.
- Butz, A., Guerlet, S., Hasekamp, O., Schepers, D., Galli, A., Aben, I., Frankenberg, C., Hartmann, J.-M., Tran, H., and Kuze, A.: Toward
380 accurate CO₂ and CH₄ observations from GOSAT, *Geophysical Research Letters*, 38, 2011.
- Colorado School of Mines Earth Observation Group: Nightfire V3.0: Nighttime Detection and Characterization of Combustion Sources, Available at https://eogdata.mines.edu/download_viirs_fire.html, 2020.
- Commission, E., Centre, J. R., Olivier, J., Guizzardi, D., Schaaf, E., Solazzo, E., Crippa, M., Vignati, E., Banja, M., Muntean, M., Grassi, G., Monforti-Ferrario, F., and Rossi, S.: GHG emissions of all world : 2021 report, Publications Office of the European Union,
385 <https://doi.org/doi/10.2760/173513>, 2021.
- Crippa, M., Guizzardi, D., Muntean, M., Schaaf, E., Lo Vullo, E., et al.: EDGAR v6. 0 greenhouse gas emissions [Dataset]. European Commission, Joint Research Centre (JRC) PID, 2021.
- Crippa, M., Guizzardi, D., Banja, M., Solazzo, E., Muntean, M., Schaaf, E., Pagani, F., Monforti-Ferrario, F., Olivier, J., Quadrelli, R., et al.: CO₂ emissions of all world countries, Luxembourg: Publications Office of the European Union. doi, 10, 730 164, 2022.
- 390 Elvidge, C. D., Zhizhin, M., Hsu, F.-C., and Baugh, K. E.: VIIRS nightfire: Satellite pyrometry at night, *Remote Sensing*, 5, 4423–4449, 2013.
- Elvidge, C. D., Zhizhin, M., Baugh, K., Hsu, F.-C., and Ghosh, T.: Methods for global survey of natural gas flaring from visible infrared imaging radiometer suite data, *Energies*, 9, 14, 2016.
- Escalona, A. and Mann, P.: An overview of the petroleum system of Maracaibo Basin, *AAPG Bulletin*, 90, 657–678,
395 <https://doi.org/10.1306/10140505038>, 2006.
- Frankenberg, C., Meirink, J. F., van Weele, M., Platt, U., and Wagner, T.: Assessing Methane Emissions from Global Space-Borne Observations, *Science*, 308, 1010–1014, <https://doi.org/10.1126/science.1106644>, 2005.
- Frankenberg, C., Meirink, J., Bergamaschi, P., Goede, A., Heimann, M., Körner, S., Platt, U., van Weele, M., and Wagner, T.: Satellite cartography of atmospheric methane from SCIAMACHY on board ENVISAT: Analysis of the years 2003 and 2004, *Journal of Geophysical*
400 *Research: Atmospheres*, 111, 2006.



- Frankenberg, C., Aben, I., Bergamaschi, P., Dlugokencky, E., Van Hees, R., Houweling, S., Van Der Meer, P., Snel, R., and Tol, P.: Global column-averaged methane mixing ratios from 2003 to 2009 as derived from SCIAMACHY: Trends and variability, *Journal of Geophysical Research: Atmospheres*, 116, 2011.
- González-Longatt, F., Serrano González, J., Burgos Payán, M., and Riquelme Santos, J. M.: Wind-resource atlas of
405 Venezuela based on on-site anemometry observation, *Renewable and Sustainable Energy Reviews*, 39, 898–911, <https://doi.org/https://doi.org/10.1016/j.rser.2014.07.172>, 2014.
- Hansen, P. C.: The L-curve and its use in the numerical treatment of inverse problems, 1999.
- Hersbach, H., Bell, B., Berrisford, P., Hirahara, S., Horányi, A., Muñoz-Sabater, J., Nicolas, J., Peubey, C., Radu, R., Schepers, D., Simons, A., Soci, C., Abdalla, S., Abellan, X., Balsamo, G., Bechtold, P., Biavati, G., Bidlot, J., Bonavita, M., De Chiara, G., Dahlgren,
410 P., Dee, D., Diamantakis, M., Dragani, R., Flemming, J., Forbes, R., Fuentes, M., Geer, A., Haimberger, L., Healy, S., Hogan, R. J., Hólm, E., Janisková, M., Keeley, S., Laloyaux, P., Lopez, P., Lupu, C., Radnoti, G., de Rosnay, P., Rozum, I., Vamborg, F., Villaume, S., and Thépaut, J.-N.: The ERA5 global reanalysis, *Quarterly Journal of the Royal Meteorological Society*, 146, 1999–2049, <https://doi.org/https://doi.org/10.1002/qj.3803>, 2020.
- Hu, C., Müller-Karger, F. E., Taylor, C. J., Myhre, D., Murch, B., Odriozola, A. L., and Godoy, G.: MODIS detects oil spills in Lake Maracaibo, Venezuela, *Eos, Transactions American Geophysical Union*, 84, 313–319, <https://doi.org/https://doi.org/10.1029/2003EO330002>,
415 2003.
- Jacob, D. J., Turner, A. J., Maasackers, J. D., Sheng, J., Sun, K., Liu, X., Chance, K., Aben, I., McKeever, J., and Frankenberg, C.: Satellite observations of atmospheric methane and their value for quantifying methane emissions, *Atmospheric Chemistry and Physics*, 16, 14 371–14 396, 2016.
- 420 Kleipool, Q., Jongma, R., Gloudemans, A., Schrijver, H., Lichtenberg, G., Van Hees, R., Maurellis, A., and Hoogeveen, R.: In-flight proton-induced radiation damage to SCIAMACHY’s extended-wavelength InGaAs near-infrared detectors, *Infrared physics & technology*, 50, 30–37, 2007.
- Koffi, E. N. and Bergamaschi, P.: Evaluation of Copernicus Atmosphere Monitoring Service methane products, Tech. Rep. EUR 29349 EN, European Commission Joint Research Centre, 2018.
- 425 Kuze, A., Suto, H., Shiomi, K., Kawakami, S., Tanaka, M., Ueda, Y., Deguchi, A., Yoshida, J., Yamamoto, Y., Kataoka, F., et al.: Update on GOSAT TANSO-FTS performance, operations, and data products after more than 6 years in space, *Atmospheric Measurement Techniques*, 9, 2445–2461, 2016.
- Lorente, A., Borsdorff, T., Butz, A., Hasekamp, O., aan de Brugh, J., Schneider, A., Wu, L., Hase, F., Kivi, R., Wunch, D., Pollard, D. F., Shiomi, K., Deutscher, N. M., Velasco, V. A., Roehl, C. M., Wennberg, P. O., Warneke, T., and Landgraf, J.: Methane retrieved from
430 TROPOMI: improvement of the data product and validation of the first 2 years of measurements, *Atmospheric Measurement Techniques*, 14, 665–684, <https://doi.org/10.5194/amt-14-665-2021>, 2021.
- Lorente, A., Borsdorff, T., Martinez-Velarte, M. C., and Landgraf, J.: Accounting for surface reflectance spectral features in TROPOMI methane retrievals, *Atmospheric Measurement Techniques*, 16, 1597–1608, <https://doi.org/10.5194/amt-16-1597-2023>, 2023.
- Lu, X., Jacob, D. J., Zhang, Y., Maasackers, J. D., Sulprizio, M. P., Shen, L., Qu, Z., Scarpelli, T. R., Nesser, H., Yantosca, R. M., Sheng,
435 J., Andrews, A., Parker, R. J., Boesch, H., Bloom, A. A., and Ma, S.: Global methane budget and trend, 2010–2017: complementarity of inverse analyses using in situ (GLOBALVIEWplus CH₄ ObsPack) and satellite (GOSAT) observations, *Atmospheric Chemistry and Physics*, 21, 4637–4657, <https://doi.org/10.5194/acp-21-4637-2021>, 2021.



- Maasakkers, J. D., Jacob, D. J., Sulprizio, M. P., Scarpelli, T. R., Nesser, H., Sheng, J.-X., Zhang, Y., Hersher, M., Bloom, A. A., Bowman, K. W., Worden, J. R., Janssens-Maenhout, G., and Parker, R. J.: Global distribution of methane emissions, emission trends, and OH concentrations and trends inferred from an inversion of GOSAT satellite data for 2010–2015, *Atmospheric Chemistry and Physics*, 19, 7859–7881, <https://doi.org/10.5194/acp-19-7859-2019>, 2019.
- Maasakkers, J. D., Omara, M., Gautam, R., Lorente, A., Pandey, S., Tol, P., Borsdorff, T., Houweling, S., and Aben, I.: Reconstructing and quantifying methane emissions from the full duration of a 38-day natural gas well blowout using space-based observations, *Remote Sensing of Environment*, 270, 112 755, <https://doi.org/https://doi.org/10.1016/j.rse.2021.112755>, 2022.
- Molod, A., Takacs, L., Suarez, M., Bacmeister, J., Song, I.-S., and Eichmann, A.: The GEOS-5 atmospheric general circulation model: Mean climate and development from MERRA to Fortuna, 2012.
- Murguia-Flores, F., Arndt, S., Ganesan, A. L., Murray-Tortarolo, G., and Hornibrook, E. R. C.: Soil Methanotrophy Model (MeMo v1.0): a process-based model to quantify global uptake of atmospheric methane by soil, *Geoscientific Model Development*, 11, 2009–2032, <https://doi.org/10.5194/gmd-11-2009-2018>, 2018.
- NASA: Troubled Waters, Article by Michael Carlowicz, available at: <https://earthobservatory.nasa.gov/images/148894/troubled-waters>, 2021.
- National Centre for Environmental Prediction: NCEP FNL Operational Model Global Tropospheric Analyses, <https://doi.org/10.5065/D6M043C6>, 2000.
- Parker, R. and Boesch, H.: University of Leicester GOSAT Proxy XCH4 v9.0, Centre for Environmental Data Analysis, <https://doi.org/doi:10.5285/18ef8247f52a4cb6a14013f8235cc1eb>, 07 May 2020.
- Powers, J. G., Klemp, J. B., Skamarock, W. C., Davis, C. A., Dudhia, J., Gill, D. O., Coen, J. L., Gochis, D. J., Ahmadov, R., Peckham, S. E., Grell, G. A., Michalakes, J., Trahan, S., Benjamin, S. G., Alexander, C. R., Dimego, G. J., Wang, W., Schwartz, C. S., Romine, G. S., Liu, Z., Snyder, C., Chen, F., Barlage, M. J., Yu, W., and Duda, M. G.: The Weather Research and Forecasting Model: Overview, System Efforts, and Future Directions, *Bulletin of the American Meteorological Society*, 98, 1717–1737, <https://doi.org/10.1175/BAMS-D-15-00308.1>, 2017.
- Qu, Z., Jacob, D. J., Shen, L., Lu, X., Zhang, Y., Scarpelli, T. R., Nesser, H., Sulprizio, M. P., Maasakkers, J. D., Bloom, A. A., et al.: Global distribution of methane emissions: a comparative inverse analysis of observations from the TROPOMI and GOSAT satellite instruments, *Atmospheric Chemistry and Physics*, 21, 14 159–14 175, 2021.
- Randerson, J., Van Der Werf, G., Giglio, L., Collatz, G., and Kasibhatla, P.: Global Fire Emissions Database, Version 4,(GFEDv4), ORNL DAAC, Oak Ridge, Tennessee, USA, 2018.
- República Bolivariana De Venezuela: Segunda Comunicación Nacional ante la Convención Marco de las Naciones Unidas sobre Cambio Climático, Available at: <https://unfccc.int/documents/89289>, 2017.
- Rystad Energy: Rystad Energy UCube Upstream Database, Oslo: Rystad Energy.(<http://www.rystadenergy.com/Databases/UCube>), 2022.
- Scarpelli, T. R., Jacob, D. J., Maasakkers, J. D., Sulprizio, M. P., Sheng, J.-X., Rose, K., Romeo, L., Worden, J. R., and Janssens-Maenhout, G.: A global gridded (0.1 x 0.1) inventory of methane emissions from oil, gas, and coal exploitation based on national reports to the United Nations Framework Convention on Climate Change, *Earth System Science Data*, 12, 563–575, <https://doi.org/10.5194/essd-12-563-2020>, 2020.
- Scarpelli, T. R., Jacob, D. J., Grossman, S., Lu, X., Qu, Z., Sulprizio, M. P., Zhang, Y., Reuland, F., Gordon, D., and Worden, J. R.: Updated Global Fuel Exploitation Inventory (GFEL) for methane emissions from the oil, gas, and coal sectors: evaluation with inversions



- 475 of atmospheric methane observations, *Atmospheric Chemistry and Physics*, 22, 3235–3249, <https://doi.org/10.5194/acp-22-3235-2022>, 2022.
- Schepers, D., Guerlet, S., Butz, A., Landgraf, J., Frankenberg, C., Hasekamp, O., Blavier, J.-F., Deutscher, N., Griffith, D., Hase, F., et al.: Methane retrievals from Greenhouse Gases Observing Satellite (GOSAT) shortwave infrared measurements: Performance comparison of proxy and physics retrieval algorithms, *Journal of Geophysical Research: Atmospheres*, 117, 2012.
- 480 Schneising, O., Buchwitz, M., Reuter, M., Vanselow, S., Bovensmann, H., and Burrows, J. P.: Remote sensing of methane leakage from natural gas and petroleum systems revisited, *Atmospheric Chemistry and Physics*, 20, 9169–9182, 2020.
- Schuit, B. J., Maasackers, J. D., Bijl, P., Mahapatra, G., Van den Berg, A.-W., Pandey, S., Lorente, A., Borsdorff, T., Houweling, S., Varon, D. J., McKeever, J., Jervis, D., Girard, M., Irakulis-Loitxate, I., Gorroño, J., Guanter, L., Cusworth, D. H., and Aben, I.: Automated detection and monitoring of methane super-emitters using satellite data, *Atmospheric Chemistry and Physics Discussions*, 2023, 1–47, 485 <https://doi.org/10.5194/acp-2022-862>, 2023.
- Shen, L., Zavala-Araiza, D., Gautam, R., Omara, M., Scarpelli, T., Sheng, J., Sulprizio, M. P., Zhuang, J., Zhang, Y., Qu, Z., Lu, X., Hamburg, S. P., and Jacob, D. J.: Unravelling a large methane emission discrepancy in Mexico using satellite observations, *Remote Sensing of Environment*, 260, 112 461, <https://doi.org/https://doi.org/10.1016/j.rse.2021.112461>, 2021.
- Skamarock, W. C., Klemp, J. B., Dudhia, J., Gill, D. O., Liu, Z., Berner, J., Wang, W., Powers, J. G., Duda, M. G., Barker, D. M., and Huang, 490 X.-Y.: A description of the advanced research WRF Model version 4, No. NCAR/TN-556+STR, <https://doi.org/10.5065/1dfh-6p97>, report available from file:///C:/Users/Stefanie/AppData/Local/Temp/PDF%20datastream.pdf, last accessed 30 Nov 2020, 2019.
- Suto, H., Kataoka, F., Kikuchi, N., Knuteson, R. O., Butz, A., Haun, M., Buijs, H., Shiomi, K., Imai, H., and Kuze, A.: Thermal and near-infrared sensor for carbon observation Fourier transform spectrometer-2 (TANSO-FTS-2) on the Greenhouse gases Observing SATellite-2 (GOSAT-2) during its first year in orbit, *Atmospheric Measurement Techniques*, 14, 2013–2039, [https://doi.org/10.5194/amt-14-2013-](https://doi.org/10.5194/amt-14-2013-2021) 495 2021, 2021.
- U.S. Energy Information Administration: Country Analysis Executive Summary: Venezuela, Available at: https://www.eia.gov/international/content/analysis/countries_long/Venezuela/venezuela_exe.pdf, 2020.
- Varon, D. J., Jacob, D. J., Sulprizio, M., Estrada, L. A., Downs, W. B., Shen, L., Hancock, S. E., Nesser, H., Qu, Z., Penn, E., Chen, Z., Lu, X., Lorente, A., Tewari, A., and Randles, C. A.: Integrated Methane Inversion (IMI 1.0): a user-friendly, cloud-based facility for 500 inferring high-resolution methane emissions from TROPOMI satellite observations, *Geoscientific Model Development*, 15, 5787–5805, <https://doi.org/10.5194/gmd-15-5787-2022>, 2022.
- Veefkind, J., Aben, I., McMullan, K., Förster, H., de Vries, J., Otter, G., Claas, J., Eskes, H., de Haan, J., Kleipool, Q., van Weele, M., Hasekamp, O., Hoogeveen, R., Landgraf, J., Snel, R., Tol, P., Ingmann, P., Voors, R., Kruizinga, B., Vink, R., Visser, H., and Levelt, P.: TROPOMI on the ESA Sentinel-5 Precursor: A GMES mission for global observations of the at- 505 mospheric composition for climate, air quality and ozone layer applications, *Remote Sensing of Environment*, 120, 70 – 83, <https://doi.org/https://doi.org/10.1016/j.rse.2011.09.027>, the Sentinel Missions - New Opportunities for Science, 2012.
- Worden, J. R., Cusworth, D. H., Qu, Z., Yin, Y., Zhang, Y., Bloom, A. A., Ma, S., Byrne, B. K., Scarpelli, T., Maasackers, J. D., Crisp, D., Duren, R., and Jacob, D. J.: The 2019 methane budget and uncertainties at 1° resolution and each country through Bayesian integration Of GOSAT total column methane data 510 and a priori inventory estimates, *Atmospheric Chemistry and Physics*, 22, 6811–6841, <https://doi.org/10.5194/acp-22-6811-2022>, 2022.



- Wunch, D., Toon, G. C., Blavier, J.-F. L., Washenfelder, R. A., Notholt, J., Connor, B. J., Griffith, D. W., Sherlock, V., and Wennberg, P. O.: The total carbon column observing network, *Philosophical Transactions of the Royal Society of London A: Mathematical, Physical and Engineering Sciences*, 369, 2087–2112, 2011.
- 515 Yu, X., Millet, D. B., Henze, D. K., Turner, A. J., Delgado, A. L., Bloom, A. A., and Sheng, J.: A high-resolution satellite-based map of global methane emissions reveals missing wetland, fossil fuel, and monsoon sources, *Atmospheric Chemistry and Physics*, 23, 3325–3346, <https://doi.org/10.5194/acp-23-3325-2023>, 2023.
- Zhang, Y., Gautam, R., Pandey, S., Omara, M., Maasackers, J. D., Sadavarte, P., Lyon, D., Nesser, H., Sulprizio, M. P., Varon, D. J., Zhang, R., Houweling, S., Zavala-Araiza, D., Alvarez, R. A., Lorente, A., Hamburg, S. P., Aben, I., and Jacob, D. J.: Quantifying methane emissions
520 from the largest oil-producing basin in the United States from space, *Science Advances*, 6, <https://doi.org/10.1126/sciadv.aaz5120>, 2020.